



## Fabricating mechanically improved silk-based vascular grafts by solution control of the gel-spinning process



Maria Rodriguez<sup>a,1</sup>, Jonathan A. Kluge<sup>a,1</sup>, Daniel Smoot<sup>a,1</sup>, Matthew A. Kluge<sup>a</sup>, Daniel F. Schmidt<sup>b,c</sup>, Christopher R. Paetsch<sup>d</sup>, Peter S. Kim<sup>e,\*\*</sup>, David L. Kaplan<sup>a,\*</sup>

<sup>a</sup> Tufts University, Department of Biomedical Engineering, 4 Colby Street, Medford, MA, 02155, USA

<sup>b</sup> Department of Plastics Engineering, University of Massachusetts Lowell, Lowell, MA, 01854, USA

<sup>c</sup> Department of Materials Research & Technology, Luxembourg Institute of Science & Technology, L-4940, Hautcharage, Luxembourg

<sup>d</sup> Tufts University, Department of Civil Engineering, 200 College Avenue, Medford, MA, 02155, USA

<sup>e</sup> Divisions of Plastic Surgery and Otolaryngology, Beth Israel Deaconess Medical Center, Harvard Medical School, Boston, MA, 02215, USA

### ARTICLE INFO

#### Keywords:

Vascular grafts

Silk

Porosity

Mechanical properties

### ABSTRACT

There is a large unmet need for off-the-shelf biomaterial options to supplant venous autografts in bypass and reconstructive surgical procedures. Existing graft alternatives formed from non-degradable synthetic polymers are not capable of maintaining long-term patency and are thus not indicated for < 6 mm inner diameter bypass procedures. To fill this void, degradable silk-based biomaterials have been proposed that can maintain their mechanical properties (i.e. compliance) while facilitating slow but progressive biomaterial remodeling and host integration mediated by cellular colonization. The goal of the present study was to enhance the porosity of gel-spun silk tubes, to facilitate faster degradation rates and improve cellularity, and thus improve host integration over time *in vivo*, while maintaining requisite mechanical functions. Silk solutions with a range of molecular weight distributions and, in turn, viscosities were used to generate tubes of varying porosities. A decrease in solution concentration correlated with an increase in mean pore size and overall porosity through a density-dependent mechanism. Tubes were mechanically analyzed, and these properties were the basis of an analytical model used to correlate tube formulations to structural compliance, which were shown to be similar to the saphenous vein. Tubes were also tested for suture retention to ensure surgical utility despite increased porosity. Tubes were implanted in the abdominal aorta of Sprague-Dawley rats via an end-to-end anastomosis model. Tubes with higher porosities showed early improvements in cell colonization that progressively increased over time; conversely, the dense architecture of less porous grafts (20MB) inhibited cell ingrowth and resulted in minimal biomaterial degradation at the 6-month time point. None of the highly porous tubes (5 MB and 10MB) remained patent at 6 months, likely due remodeling inducing bulk mechanical failure or a compromised blood-material interface.

### 1. Introduction and background

The search for improved grafting options has been extensive, covering a range of material choices, formats, and means to integrate with the host vasculature. As one important factor, graft pore structure (pore type, size, and interconnectedness) can impact long-term patency by mediating cellular infiltration [1,2] clotting kinetics, and anchoring of the neointima via alterations to the surface topography [3]. Changes to the pore architecture of vascular implants can also influence their mechanical properties [4]. With decreases in overall solids density,

thinner pore walls will be less resistive to buckling under external loads, and thus behave as more compliant structures [5]. In turn, a more compliant graft wall structure that can match native tissue responses to flow has been shown to decrease rates of neointimal hyperplasia following implantation and thus promote long-term patency [6]. Direct evidence in the literature that this “compliance-matching” phenomenon can be maintained over long time periods *in vivo* is seldom reported for biodegradable grafts due to the contradictory requirements of degradation, cellular remodeling, and mechanics [7].

Degradable biomaterials made from silk fibroin that can serve as

\* Corresponding author.

\*\* Corresponding author.

E-mail addresses: [peter\\_kim@atriushealth.org](mailto:peter_kim@atriushealth.org) (P.S. Kim), [david.kaplan@tufts.edu](mailto:david.kaplan@tufts.edu) (D.L. Kaplan).

<sup>1</sup> These authors contributed equally to the work.

alternatives to the clinically-approved synthetic grafts were investigated in this study. Unlike synthetic polymers, naturally derived biopolymers can offer improved cytocompatibility and biocompatibility due to the presence of embedded structural and functional molecules [8]. Several studies have shown that silk fibroin has properties that make it ideal for vascular applications such as controllable biodegradability, minimal inflammatory reactions, and suitable mechanical properties [9–11]. Silk-derived grafts have been fabricated using multiple spinning approaches, resulting in tubes with diverse mechanical features [12,13] and architectures supportive of vascular cell colonization *in vivo* [14]. Preliminary short-term *in vivo* assessment indicated that the tubes could support the development of distinct intraluminal smooth muscle cell and endothelial cell layers; however, observations at 1 month suggested restricted silk material remodeling and cell ingress due to the density of the tube wall [14]. Therefore, the goal of this work was to construct gel-spun silk grafts with enhanced porosity and faster degradability to accelerate cell colonization and extracellular matrix deposition. A silk-based material system offering stable mechanical features and now a means of accelerating cell and tissue ingress could become a compelling off-the-shelf graft alternative.

To fabricate more porous tubes, gel-spinning was employed for its versatility in generating layered materials of controllable properties. The gel-spinning process relies on high concentration (i.e. > 20% w/v) silk solutions. Once extruded, the more viscous silk is metastable due to increased crystallinity and thus maintains its tubular shape profile and association with the spinning mandrel [12]. Lyophilizing tubes generated with high concentration silks (using a rapid initial freeze rate and low freezing temperature set point for primary drying) prior to inducing additional crystallinity resulted in a broad, but small pore architecture. In this work we hypothesized that solutions of lower concentration, but higher molecular weight would be both spinnable and generate tubes that, when lyophilized, would result in increased porosity and pore sizes. These high molecular weight solutions were generated through control of silk extraction conditions [15,16]. The resulting conduits formed after lyophilization were characterized structurally, mechanically, and biochemically for vascular-specific functions. Additionally, the morphology of the residual silk grafts and cellularity 1–6 months after implantation in the rat model were evaluated to appreciate both short- and long-term remodeling behavior influenced by tube structure. These pilot *in vivo* studies provided preliminary data regarding the kinetics of cell ingress and rates of material remodeling, prior to evaluating compliance matching in larger animal models [17].

## 2. Materials and methods

### 2.1. Silk solution preparation

Silk fibroin solutions were prepared as reported previously [18]. *Bombyx mori* silkworm cocoons were supplied by Tajima Shoji Co., LTD (Yokohama, Japan). Briefly, pure silk fibroin was extracted from cocoons by boiling in a sodium carbonate solution (0.02 M) (Sigma-Aldrich, St. Louis, MO) for 5, 10, 20, or 30 min to remove sericin, referred to as minute boil (MB). Per previous studies the molecular weight of silk fibroin can be correlated to this extraction time [15]. The purified silk fibroin was solubilized in aqueous lithium bromide (9.3 M) (Sigma-Aldrich, St. Louis, MO) for 4 h at 60 °C. The 5- and 10-min extracted silk fibers were dissolved in lithium bromide solution at 15% w/v protein concentration, while 20- and 30-min extracted fibers were dissolved at 20% w/v. The silk fibroin solutions were dialyzed using 3.5 kDa MW cutoff Slide-A-Lyzer™ Cassettes (Life Technologies) against deionized water for 48 h. The concentration of the silk solution was determined by drying a known volume of the solution and assessing the mass of the remaining solids (typically 6–8% w/v). These silk solutions were stored at 4 °C prior to use. To increase the concentration of silk solutions they were first subject to dehydration in Slide-A-Lyzer Cassettes open to the ambient (50% relative humidity) environment for upwards of 16 h. The

concentration of the silk solution was determined according to the method described above, drying a known volume of the solution and assessing the mass of the remaining solids to obtain % w/v concentration. If higher concentration were further required a CentriVap Vacuum Concentrators (Labconco, Kansas City, MO) was used with 2 mL vials.

### 2.2. Viscosity of silk solutions

Molecular weight (MW) of silk fibroin solutions can be correlated to boiling time (MB), 5–10 MB solutions have approximate MWs of 171–460 KDa [19] and 15–30 MB solutions have approximate MWs below 160 KDa [20,21]. Viscosity of silk solutions prepared using variable boiling times (5–30 MB) and concentrations (5%–25% w/v) were measured by a Brookfield™ DV-II + Pro Viscometer with a Wells-Brookfield Cone/Plate adaptor. For each test, a 500 µL aliquot was placed under a CPE-52 cone (3° angle, 12 mm diameter) onto a CPE-44PY cup. The cone rotated continuously at a shear rate ranging from  $0.1 \text{ s}^{-1}$  to  $10 \text{ s}^{-1}$  for 5 s per step to reach equilibrium. Data was collected at 15-s intervals using Rheocalc (V3.3, Build 49.1) software. Recorded torque values were converted to shear stress, plotted against varying shear rate, and fit by Bingham Flow model via linear regression from which the value of plastic viscosity was obtained. All samples yielded a fit with  $r^2 \geq 0.95$ , suggesting an appropriate range of shear rates were used throughout.

### 2.3. Gel-spinning

A custom silk gel spinning device was used to fabricate the tubes as previously described [12]. Optimal process parameters (winding patterns, axial and rotational speeds) were determined previously [12]. Briefly, rotational and axial slew rates of the rotating mandrel and needle gauges (25–30 G) were tailored for each feedstock solution to maintain consistent and uninterrupted gel coverage during the spinning process. To make tubes, the spinning mandrel was coated with Teflon and had an outer diameter of 1.29 mm (McMaster-Carr). Once covered with two passes of gel, tubes were immediately transferred to a pre-cooled shelf set to  $-25 \text{ °C}$  within a VirTis Genesis 25 L Super XL Freezer-Dryer (SP Scientific, Stone Ridge, NY) and were lyophilized using a protocol previously described [16]. Once the lyophilizer chamber had achieved convergence of the pirani gauge and capacitance manometer pressure readings the tubes were considered fully dry and removed from the lyophilizer. After a one-hour treatment with 90% (v/v) methanol/water, the gel-spun tube was removed from the Teflon-coated mandrel. This previously established method was used to prepare silk tubes matching the size of abdominal aorta in Sprague-Dawley rat (inner diameter 1.0–1.5 mm, length 20 mm, wall thickness 0.1 mm) [14].

### 2.4. Morphological characterization

Scanning Electron Microscopy was used to visualize the inner luminal surface morphology of the tubes and their cross-sections. Sections were prepared by freeze-fracturing under liquid nitrogen. All samples for SEM were sputter-coated with gold using a Polaron SC502 Sputter Coater (Fisons, VG Microtech, East Sussex, England) and imaged using a Zeiss EVO MA10 electron microscope (Carl Zeiss AG, Germany) using a solid state secondary electron detector, and an accelerating voltage of 3 kV.

### 2.5. Degradation testing

Degradation of silk fibroin biomaterials has previously been studied using protease XIV [15]. Silk gel spun tubes weighing 10 mg from either 5, 10, 20, or 30 min extraction formulations were subjected to protease XIV enzymatic degradation under continuous orbital shaking in an

incubator set to 37 °C. Lyophilized protease XIV powder (Sigma-Aldrich, St. Louis, MO) was reconstituted to 1 mg/mL (0.1 U/mL in 1X PBS) with continuous stirring for 1 h. Tubes were incubated in 750 µL protease solution for 14 days with complete enzyme changes occurring on days 2, 4, 7, and 10. Each day, one set of samples (N = 4) was removed, rinsed for 15 s in deionized water, followed by 2 min of orbital shaking in fresh deionized water to completely remove enzyme and silk breakdown products. Samples were dried in a fume hood overnight to compare weights at each time point to original starting tube weights.

## 2.6. Mercury intrusion porosimetry

Mercury intrusion porosimetry (MIP) measurements were conducted to evaluate the porosity and pore size distribution of gel-spun tubes. Two-pass tube sections measuring ~10 mg were analyzed via a Quantachrome PoreMaster mercury intrusion porosimeter (Quantachrome Instruments, Boynton Beach, FL). For each formulation, samples were weighed, and subsections pooled into glass sample cells with a 0.5 cc stem volume. A low-pressure cycle (max pressure: 50 psi, or 344 kPa) was performed to evaluate pore sizes between four and several hundred microns. Each sample cell was then transferred to an oil-filled hydraulic chamber for further intrusion over a pressure range of 20–33,000 psi. Results are reported as a histogram of pore size (in µm) vs. a pore size distribution function, FV, where  $FV = - [dV/d\log(D)]$ , V is the cumulative pore volume, and D is the pore diameter. Pore size, pore size distribution, and total intruded volume were averaged over the volume of one scaffold. To determine porosity, the skeletal density of the silk scaffold was assumed to be 1.31 g/cm<sup>3</sup> based on previous methods [15].

## 2.7. Uniaxial mechanical characterization

To characterize the mechanical properties of the wall material, and later use this to generate an analytical model, strips were generated on larger 50 mm diameter aluminum mandrels on which samples could be lyophilized in the same manner by which the gel-spun tubes were generated. Uniaxial tensile properties were determined on fabricated testing strips 2–9 mm wide × 20–30 mm long. Additional strips culled from adjacent sections of the sample were pre-conditioned in water, fixed in formalin and then processed through a series of alcohol dehydration solvents before paraffin embedding, sectioned and then imaged to capture the cross-sectional area of the strips in a hydrated state. Imaging software (National Instruments Vision Development Module, 2009) was used to determine width and thickness of these samples. Tensile characterization was performed for a range of silk formulations to determine the difference in properties as a function of molecular weight and concentration. The tensile measurements were captured using an Instron 3366 Load Frame (5 N and 10 N load cells). The testing was performed in a phosphate-buffered saline (PBS) bath at 37 °C. A preload on 0.02 N was used to account for specimen straightening followed by a strain rate of 0.01%·min<sup>-1</sup>. The video axial and video transverse strains were measured based on two fiducial marker dots placed 10 mm apart in both axial and transverse directions, forming a crucible shape. An Advanced Video Extensometer (AVE) was used to track deformations in axial and transverse directions which were recorded concurrently with force measurements using Bluehill Software (Ver. 3.0, Instron). Force data was converted to stress based on cross sectional area measurements and strain taken from the AVE data to plot stress-strain curves. Young's modulus was calculated from the slope of the linear region of the stress-strain curves at the small strain level (below 5%) that would be expected under physiological conditions [23]. The Poisson's ratio was calculated as the ratio of strain in transverse direction ( $\epsilon_{trans}$ ) and axial direction ( $\epsilon_{axial}$ ) from AVE data.

## 2.8. Suture retention tests

Suture Retention was tested per ANSI/AAMI/ISO Standard 7198:1998/2001/(R)2004 "Cardiovascular implants - Tubular vascular prostheses" [24]. For these tests, an Instron 3366 Load Frame was employed with a 10 N load cell. Briefly, 2 mm inner diameter tubes (20–30 mm in length) were cut transverse to the long axis into 10 mm tubular segments. An Ethicon 8.0 suture was inserted through one wall 2 mm from the end and secured to the upper tensile grip, while the lower end of the sample was clamped in the lower grip. The suture was pulled at a rate of 50 mm min<sup>-1</sup> and the force required to pull through the tube was recorded. The ultimate strength at failure was computed as the maximum force recorded before graft wall failure.

## 2.9. Compliance testing

A custom compliance tester was constructed, it was composed of a programmable syringe pump (Pump Systems Inc. model NE-1600), a holding chamber, and two in-line pressure transducers (Pendotech, PRESS-S-000). Gel spun tubes 25–30 mm length and 2 mm inner diameter were used for compliance testing. Three samples per molecular weight were tested. Tubes were attached to the inline pressure transducers using gauge 15 stainless steel blunt end dispensing needles (McMaster-Carr, Robbinsville, NJ). To assure no leaks occurred at the ends a waterproof adhesive (3M™ Wet Surface Adhesive) was used to attach the dispensing needles to the graft ends. The length of the graft after attachment was kept above 10 mm. A camera (Basler, acA4600-10uc Newtown, Pennsylvania) was used for image capture and mounted above the graft. A custom LabVIEW program (National Instruments, 2009) was written for the simultaneous image and data acquisition.

The grafts were pressurized using a steady state pressure ramp from 0 to 400 mm Hg. A syringe was filled with water containing blue dye (1 mg/mL, Brilliant Blue FCF, Viveri Food Colors, Cleveland, OH) and pumped at a flow rate of 10 mL min<sup>-1</sup> for 5 s, then held at a constant pressure for 30 s. The process was repeated incrementally until a pressure of 200 mm Hg was reached. The dye aided in establishing contrast between intimal fluid and the surrounding bath fluid to establish premature failures (if any). Images were captured at 1 frame per second. The pressure at each frame was logged onto each image file. Image post processing was performed using a NI-Vision Assistant script. Briefly, a set of ten frames per pressure condition were analyzed. For each set images were converted to binary, isolated regions of interest (ROI) were picked manually at three different axial locations. Within these ROI the outermost edges of the graft were automatically identified and the distances between the edges were measured using the "distance between edges" LabView tool. This measurement was averaged for each frame and used as the outer diameter of the graft. The compliance of the graft was calculated per the equation below, where  $D_1$  and  $D_2$  are the diameters at the first and second pressure conditions ( $P_1$  and  $P_2$ ).

Equation (1). vascular graft compliance

Graft compliance defined as the change in diameter ( $D_2 - D_1$ ) times the corresponding change in pressure ( $P_2 - P_1$ ).

$$Compliance = \left( \frac{D_2 - D_1}{D_1} \right) \times \left( \frac{P_2 - P_1}{P_1} \right) \quad (1)$$

## 2.10. Mathematical model and finite element analysis

An analytical mathematical model was first created to relate measurable material properties to the empirical measurements of compliance, defined as the change in vessel diameter over the change in pressure. This mathematical model assumed a conduit was under uniform pressure, therefore disregarding the end effects and relating it

directly to the experimental compliance measurement conditions that were performed. Then a more complex model using Finite Element Analysis (FEA) was created using ABAQUS (Dassault Systèmes, Providence, Rhode Island) of the vascular conduit to evaluate the relationship between material properties (elastic modulus) and structural properties (compliance) for a range of geometrical dimensions. The model considered a hollow cylindrical tube fixed at both ends pressurized from 0 to 200 mm Hg in increments of 0.005 mm Hg. A linear isotropic material was used to model the behavior of the porous tube wall over the entire range of modeled stresses. The longitudinal, radial and circumferential stresses were calculated using quasi-static analysis. A proof of concept parametric analysis was also done by varying the wall thicknesses from 100 to 600  $\mu\text{m}$ .

### 2.11. Implantation of tubes in rat interpositional model

Silk tubes were implanted in the abdominal aorta of Sprague-Dawley rats via an end-to-end anastomosis model [14]. Animals were cared for in compliance with Tufts University Institutional Animal Care and Use Committee (IACUC) in accordance with the Office of Laboratory Animal Welfare (OLAW) at the National Institutes of Health (NIH). Male Sprague-Dawley rats (Strain Code 400, SAS SD, Charles River) were acquired at 350 g and allowed to acclimate for at least 5 days prior to implantation. The animals were anesthetized using isoflurane (4% induction, 2.5% maintenance). Prior to surgery, the silk tubes were adjusted to meet the anatomical requirements of the rats (1.29 mm inner diameter, 0.1 mm wall thickness, 10–15 mm length). Tubes were EtO sterilized in an Anprolene sterilization system (Andersen Products, Haw River, NC) using a 12-h cycle (10 h exposure, 2 h degassing), as recommended by the manufacturer. Tubes in sterile pouches were subject to an additional 24 h degassing in a fume hood at room temperature to remove residual ethylene oxide. The surgical model involved a midline laparotomy and subsequent isolation of the infrarenal abdominal aorta. Micro clamps were used to halt blood flow and the aorta was transected and washed with saline. The silk graft was then interposed after necessary trimming of the adventitia into the native aorta and secured by 8–0 monofilament polypropylene sutures (total of 12). Target ischemia was within 30–60 min and graft patency were acutely assessed using a blanching flow-no flow technique before closing the animal. Animals were monitored daily for signs of lower limb ischemia for 3 days and then twice weekly for the remainder of the study. At various incremental time points up to 6 months, the rats were euthanized by  $\text{CO}_2$  asphyxiation and implants resected, including > 10 mm of attached vascular tissue at both ends of the anastomosis.

### 2.12. Histology and immunohistochemistry

Harvested tissues were stored in formalin for  $\geq 48$  h and then processed through a series of alcohol dehydration solvents before paraffin embedding. Samples were cut in 5  $\mu\text{m}$  sections for subsequent staining with Hematoxylin and Eosin (H&E), Verhoeff's elastic (VE), Masson's Trichrome (TC). For immunohistochemistry (IHC), antigen retrieval was used to restore antigenic epitopes then the sections were blocked with serum and incubated with anti-CD31, anti-Smooth Muscle Actin (SMA) or anti-Factor VIII (FVIII). Sections were then washed in PBS, incubated with a secondary anti-rabbit antibody for 30 min and finally with ImmPACT DAB enzyme substrate for 5 min. After washing with water, the IHC sections were counterstained with hematoxylin and mounted.

### 2.13. Statistics

Values were expressed as mean  $\pm$  SD (standard deviation) for a minimum of  $N = 3$  replicates for each group, unless otherwise indicated. Student's t-test was performed for paired observations. Statistically significant differences were determined by one- or two-way

analysis of variance (ANOVA) and the Tukey posttest. Statistical significance was accepted at the  $p < 0.05$  level and indicated in the figures as \* $p < 0.05$  or \*\* $p < 0.01$ .

## 3. Results

### 3.1. Gel spinning using low concentration and high $M_w$ fibroin solutions

When processing silk to obtain lower molecular weights the boiling time was decreased and the resulting silk solution concentration was decreased [16]. Utilizing these solutions for gel-spinning required that their concentrations be sufficiently increased to surpass a minimum viscosity threshold that allowed the resultant gel to remain associated with the collection mandrel during its continuous rotation. However, if the solutions were too heavily concentrated, they were too viscous to eject from the needle used for deposition. The flow of the silk solutions fit the behavior of a Bingham Plastic where the viscosity ( $\eta_B$ ) depends on a critical shear stress ( $\tau_0$ ) and then becomes constant. These fluids are characterized with a constant viscosity ( $\eta_B$ ) and modeled with the equation below:

#### 3.3.1. Equation (2). Bingham plastic fluid model

The Bingham plastic fluid model relates the shear stress of a fluid ( $\tau$ ) from the critical shear stress ( $\tau_0$ ), the fluid viscosity ( $\eta_B$ ) and the shear rate ( $\dot{\gamma}$ ).

$$\tau = \tau_0 + \eta_B \dot{\gamma} \quad (2)$$

Adequate spinning solutions were obtained from the 5 MB, 10 MB, 20 MB, and 30 MB groups at concentrations of 8–11%, 12–17%, 15–23%, and 20–27% (w/v), respectively (Fig. 1). The viscosity (cP) of silk solutions increased exponentially with increased concentration (% w/v), independent of the boil time used to generate the solutions. By comparing the concentration ranges required for spinning to the viscosity profiles, it appeared that a viscosity range of 500–3000 cP was universally acceptable for gel-spinning.

### 3.2. Characterization of silk tube porosity

Once these different tube systems were lyophilized, they contained vastly different pore architectures with characteristic pore sizes ranging from  $\sim 200 \mu\text{m}$  to  $\sim 20 \mu\text{m}$  for the 5 MB and 30 MB groups, respectively (Fig. 2). Pores for the 5 and 10 MB groups appeared interconnected and sheet-like while pores for the 20 and 30 MB groups appeared more spherical but isolated. This could be related to a more unimodal pore size distribution of high molecular weight (5 and 10 MB) compared to

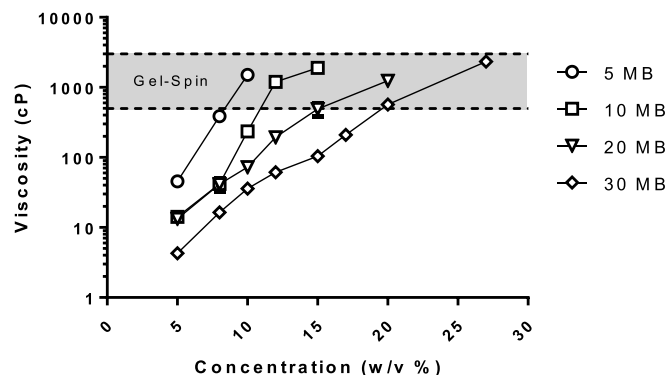
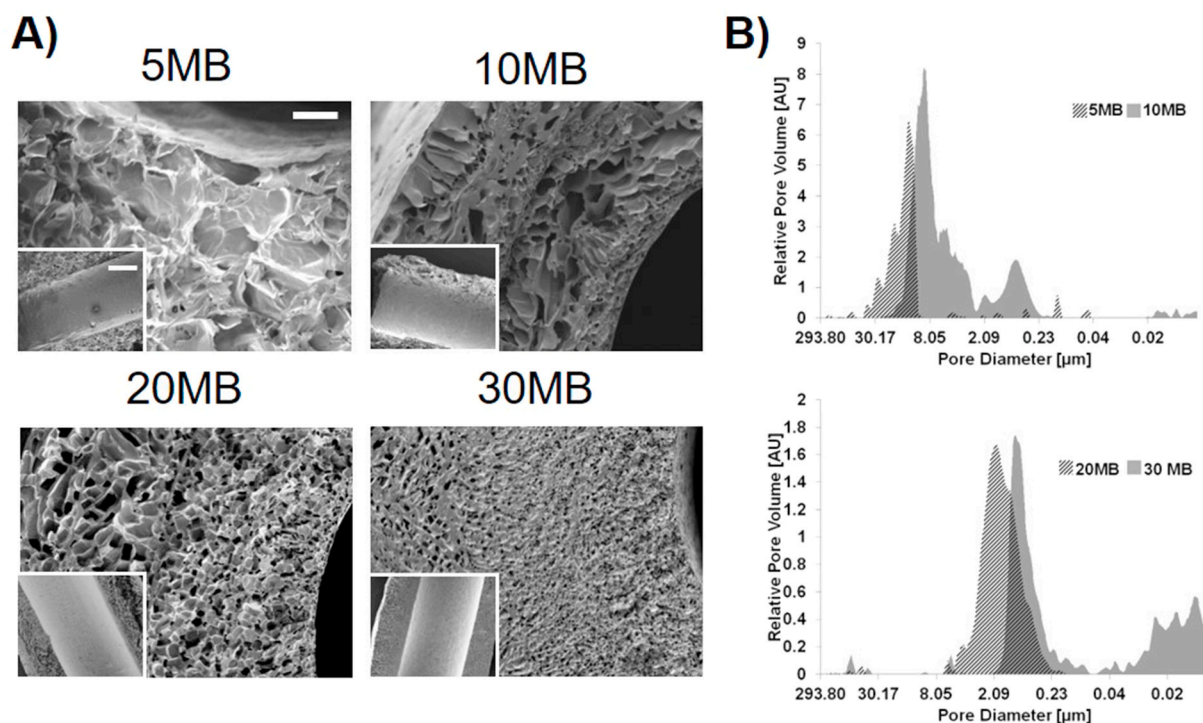


Fig. 1. Viscosity of silk solution needed for gel-spinning. Silk solutions of increasing boiling times (5 MB, 10 MB, 20 MB and 30 MB which correlate to decreasing molecular weights) and increasing concentrations were prepared. The viscosity of these silk solutions were characterized with a cone-plate viscometer. A trend of increase in viscosity with decreasing boiling time (increasing molecular weight) and increasing solution concentration was seen.



**Fig. 2. Morphological characterization of silk tubes showed control of silk solution boiling time affected tube structure.** (A) Tubes formed from 5 MB, 10MB, 20MB, 30MB, (14%,16%,26%,34% w/v concentrations, respectively) characterized by SEM showed different pore structures after lyophilization. Scale bars 100  $\mu\text{m}$  for cross-sectional images. Inset shows the inner lumen of each tube (inset scale bar = 500  $\mu\text{m}$ ). (B) Mercury Intrusion Porosimetry was used to evaluate the pore size distribution (between 10 nm and  $\sim 300 \mu\text{m}$ ) for tubes shown in panel (A). The dark hashed section of the histogram indicates the overlap between each MB group.

the bi-modal or wider distribution of the low molecular weight (20 and 30 MB). Despite these differences in pore architecture, the inner lumens of the tubes were smooth, owing to the initial collection on the smooth surface of the Teflon-coated mandrel (see inset Fig. 2A). The fast-freezing approach using a pre-cooled lyophilizer tray likely also limited the rate and extent of ice crystal nucleation required for large pore formation on the inner lumen. Gel-spun tubes formed from the 5, 10, 20, and 30 MB silk solutions resulted in distinct pore size distributions and porosities, as measured by mercury intrusion porosimetry (MIP) (Fig. 2B). For 5 MB samples the distribution of pore sizes was unimodal, between 0 and 45  $\mu\text{m}$  with some smaller interspersed pore families below 6  $\mu\text{m}$ . For 10 MB the distribution was bimodal between 0.2 – 3 and 3–20  $\mu\text{m}$ . For 20 MB the distribution was unimodal between 0.2 and 6  $\mu\text{m}$ . Finally, for 30 MB the distribution was also bimodal between 0.08 and 2  $\mu\text{m}$  and another population < 0.05  $\mu\text{m}$ . The areas of the tube closest to the cold surface (i.e. the rod) freeze the fastest, resulting in small and fairly isolated pores compared to the remaining bulk of the tube wall. The result is multiple populations of distinct pore sizes. This is why the 10 MB samples contain a subset of pores in a similar size range to the 20MB and 30MB groups. Consistent with the SEM cross-sectional images, tubes formed from 5 MB solutions had a narrow spread of large pore diameters; conversely, the bimodal distribution of the 10 MB reflected regions of both large  $\sim 10 \mu\text{m}$  and small  $\sim 1 \mu\text{m}$  pores seen by SEM. Tubes made from 20 MB to 30 MB were devoid of macroscopic pores and appeared more homogenous in cross-section, though visualization of pores in the sub-micron range (as indicated by MIP) were not achieved in this study. The total porosity of the tubes was calculated by assuming a 1.31 g/mL pore wall density and dividing the total intruded volume by the total volume (intruded + solids). Overall porosity correlated directly to pore sizes of the samples: porosity = 86.7% for 5 MB, 80.5% for 10MB, 65.4% for 20MB and 52.0% for 30MB.

### 3.3. Degradation testing

Lyophilized silk tubes of varying molecular weights were subjected to a constant enzymatic stress over a period of 14 days to evaluate relative rates of degradation. Protease 14 was changed every 2–3 days and tubes subjected to constant agitation. While tubes (5 MB) in PBS did not change mass appreciably over the 14-day study, every tube subjected to enzymes lost a significant amount of mass (Fig. 3). The fastest to degrade was the 5 MB group (52% loss) and the slowest was

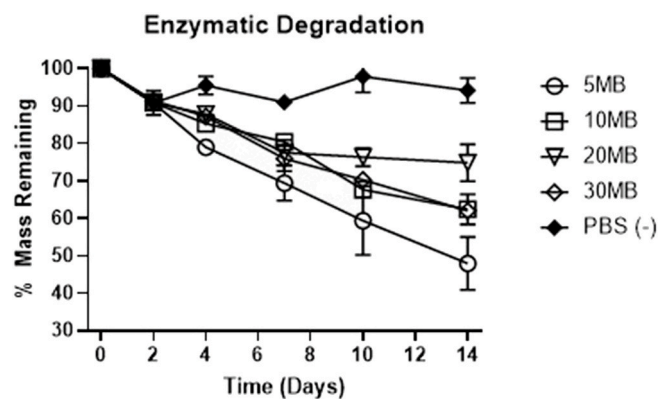


**Fig. 3. *In vitro* enzymatic degradation.** Sections of tubes (10 mg each) formed from 5MB, 10MB, 20MB, 30MB, (14%, 16%, 26%, 34% w/v concentrations, respectively) were subject to Protease XIV enzyme exposure for 14 days under conditions of constant orbital shaking. A 5MB group was subject to PBS (without enzyme) as a control. Dry tubes were weighed at the onset of the study and samples were removed from enzyme solutions, rinsed in DI water, dried and re-weighed at each time point. Enzyme solution was replaced at each measurement interval. While all groups exposed to enzyme lost mass throughout the study, the 5MB group was the fastest to degrade, likely due to rapid fluid transport through the large pores.

20MB (25%). Degradation times *in vitro* increased with increasing molecular weight due to larger pores sizes that allowed for greater enzyme diffusion. However, higher molecular weight tubes should also be more resistant to degradation. In the 20MB formulation the effects of these two opposing forces were seen, assuming consistent pore size, the pore sizes were big enough for enzyme diffusion. However, the higher molecular weight compared to the 30MB could have led to greater resistance to degradation.

### 3.4. Mechanical analysis

The lyophilized tubes had very distinct mechanical properties which varied by molecular weight and concentration. Strips formed from each molecular weight at varying concentrations within the gel-spinnable regime (Fig. 1) were mechanically tested. To attain a viscosity within the gel-spinning regime the concentration must be adjusted for each molecular weight. Therefore, in our system these two factors cannot be decoupled from each other. We increased the concentration with decreasing molecular weight to keep viscosity within gel-spinning regime and the resulting data was presented as a function of concentration. Three representative stress strain curves of low (20 MB), medium (10 MB) and high (5 MB) molecular weights (Fig. 4A) show a similar qualitative behavior between the different molecular weight constructs, with a linear region at low strains followed by a long deformation at higher strains. No significant trends were seen for strain or stress at break and therefore these were not analyzed. The elastic modulus showed a linear increasing trend with concentration (Fig. 4B) and the suture strength showed an increasing linear trend with molecular weight (Fig. 4C). The Poisson's ratio did not vary significantly with concentration or molecular weight.

### 3.5. Analytical and computational model

To further understand the relationship between material properties and graft compliance an analytical model (see Fig. 9) of a cylinder under uniform pressure (disregarding boundary conditions) was made. In this model the stress in the longitudinal direction was set to zero and only plane stresses were considered. Under these conditions initially the radial stresses were due to internal and external pressure ( $P_i$  and  $P_o$ ). Using thick walled cylinder mechanics, the radial and circumferential stresses were derived. For a linear isotropic material these stresses can be related to two material parameters: the elastic modulus and the Poisson ratio. The compliance was derived as a function of the radial displacement, the elastic modulus and the Poisson ratio. The equations used in the analytical model are detailed in Fig. 8. The estimated compliance as a function of elastic modulus with a Poisson ratio of 0.2 (blue) and 0.4 (red) are shown in Fig. 9. According to the model there was an inverse linear relationship between the elastic modulus and compliance. Increasing the molecular weight (thus altering the crystallization behavior) and decreasing the concentration resulted in a graft having a lower elastic modulus and therefore greater compliance. The characterization of the mechanical properties of the grafts showed tuneability of the elastic modulus but not of the Poisson's ratio. The analytical model did not show a significant effect of Poisson's ratio on compliance, and further analysis disregarded the effect of Poisson's ratio (fixing at 0.3 the average characterized value for further modeling work).

Finite Element Analysis (FEA) considered a more complex numerical model, representing the tube as a cylinder fixed at both ends with the longitudinal, radial and circumferential stresses calculated using quasi static analysis. Simulations varied pressure from 0 to 200 mm Hg

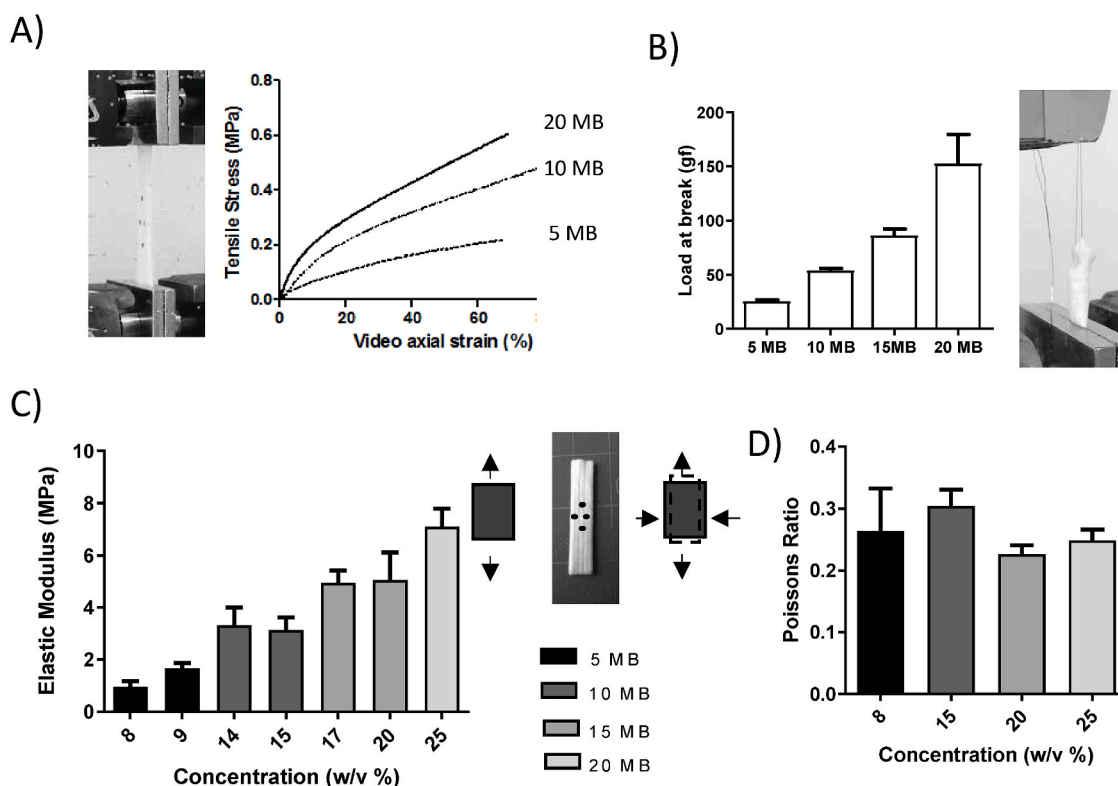


**Fig. 4.** Mechanical Properties of vascular grafts. Uniaxial tensile properties were determined for a range of silk formulations to determine the difference in properties as a function of molecular weight and concentration. Concentrations of 9% w/v for 5 MB, 14% w/v for 10MB, 17% for 15MB and 25% w/v for 20MB silk solutions were tested. (A) From the resulting stress strain curves (representative curves shown here for low (20 MB), medium (10 MB) and high (5 MB) molecular weights) the young's modulus was calculated from the slope of the linear region below 5% (C), and Poisson ratio was calculated as the ratio of transverse strain to axial strain (D). The suture retention strength (B) was defined as the force required to pull through the tube or cause the wall to fail. There was a linear trend with decreasing elastic moduli (indicative of greater elasticity) and decreasing suture retention strength as the molecular weight increased and the concentration decreased.

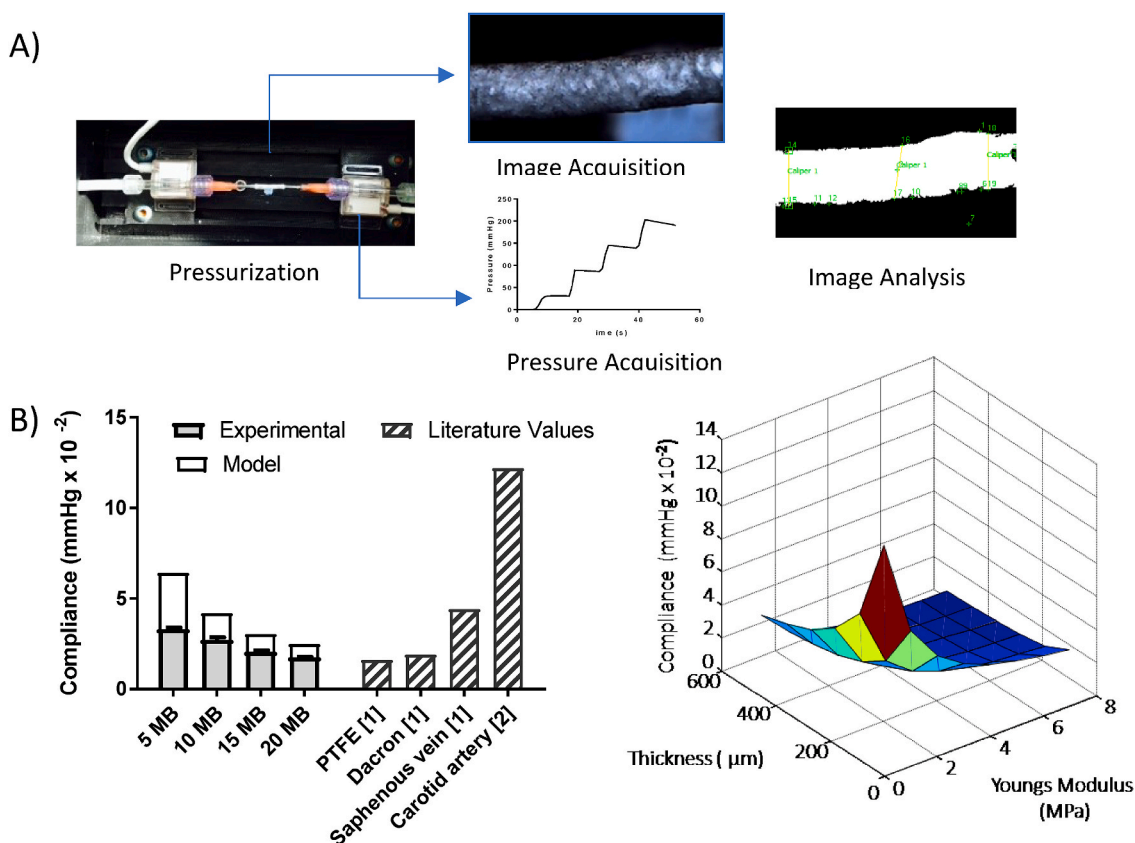


**Fig. 5.** Experimental and model compliance of vascular grafts. (A) Compliance was measured experimentally using a custom pressurization device, composed of a programmable syringe pump, a holding chamber, a camera and two in-line pressure transducers. Tubes made with concentrations of 8% w/v for 5 MB, 14% w/v for 10MB, 18% for 15MB and 25% w/v for 20MB silk solutions were tested. (B) A Finite Element Model was made using ABAQUS simulating the experimental compliance test. The model considered a cylinder fixed at both ends, the longitudinal, radial and circumferential stresses were calculated using quasi static analysis where the cylinder was pressurized from 0 to 200 mm Hg in increments of 0.005 mm Hg. The predicted compliance as a function of thickness and elastic modulus is plotted (right). The predicted compliance, experimental compliance and compliance values derived from literature are compared (left).

and wall compliance could be modified by changing the graft dimensions and/or material properties. An exemplary parameter of graft thickness was used as a proof of concept (Fig. 5B) and resulted in an inverse linear relationship with compliance (thinner graft, with a lower elastic modulus result in a lower compliance). FEA model showed that by lowering the graft thickness from 200 μm to 100 μm with an elastic modulus below 2 MPa and compliance levels above 6 mm Hg × 10<sup>-2</sup> could be achieved. The highest molecular weight graft (5 MB) had an average elastic modulus of 1 MPa and the model predicted using this formulation and controlling graft thickness compliance levels surpassing those of the saphenous vein (4 mm Hg × 10<sup>-2</sup>), the gold standard, could be reached.

### 3.6. Experimental Compliance

To validate the computational model, the compliance of the various grafts was experimentally tested (Fig. 5A). The model predicts that graft compliance is heavily influenced by tube wall thickness and modulus, the latter being dictated by the gel spinning solution concentration. Several methods are used to measure compliance using change in diameter and change in volume [25–28] in both static and dynamic conditions [29,30]. We chose to use a static compliance measuring the change in diameter to most closely relate to our mechanical model. The compliance of tubes made from four different molecular weight silks (5, 10, 15 and 20 MB) was tested using a custom compliance tester. For these experiments the average gel-spinning silk concentration for each molecular weight composition was used as a representative case (8,14,18, and 25 respectively). Trends in experimental compliance

values matched those predicted by the numerical models, with lower molecular weight showing higher compliance (Fig. 5B). However, the model predicted higher compliance values than was directly measured. It was speculated that considering more accurate end effects (consistent with the experimental set up including needles) and more accurate geometry such as a 3D scan of grafts would improve the model to match the experimental compliance. With the current system both experimentally and analytically it was demonstrated compliance levels (3.3 mm Hg × 10<sup>-2</sup>) comparable to the gold standard saphenous vein (literature reported 4 mm Hg × 10<sup>-2</sup>) and surpassing synthetic grafts such as PTFE and Dacron (Fig. 5B) could be reached.

### 3.7. Implantation of tubes in rat interpositional model and histology analysis

Silk grafts were implanted in the abdominal aorta of Sprague-Dawley rats via an end-to-end anastomosis model. The rats exhibited no signs of acute thrombosis and were monitored throughout the study for any signs of impaired health, clotting or lower limb ischemia. Twenty-one rats were used for these studies, 7 used for each of the 5, 10 and 20 MB groups. Ten rats did not survive the surgical procedure beyond 24 h, due to a surgical complication. Cause of acute death included exsanguination during the surgery, an anesthetic complication due to the long ischemic time, or loss of lower limb function requiring euthanasia immediately post-surgery. Of the 11 surviving rats, 4 rats were retrieved at either 1, 3 or 6 months and were found with fully occluded grafts (2 grafts were 5 MB, 1 was 10MB and 1 was 20MB). There were 2 rats for the 10MB group that were patent (both were recovered at 1

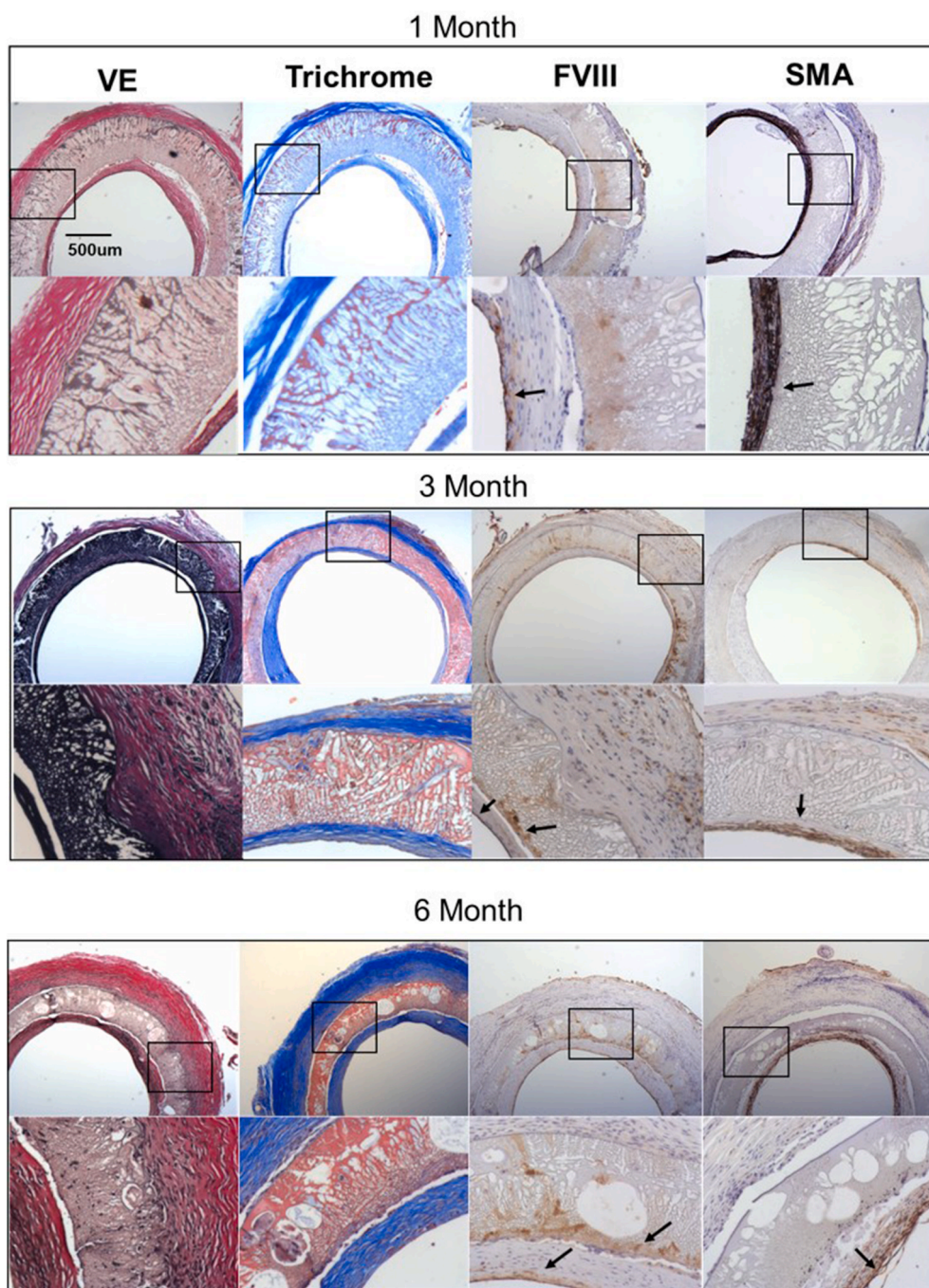


**Fig. 6.** Histological cross-sections of 20 MB grafts 1, 3- and 6-months post-implantation. Adjacent sections were stained for Verhoff's elastic (VE), trichrome, Factor VIII (FVIII) and smooth muscle actin (SMA). For each stain images are shown in low ( $20\times$ , top) and high magnification ( $40\times$ , bottom) corresponding to the box in the image above. Arrows indicate areas of clear positive IHC staining. Histology images shown were taken midgraft. The scale bar ( $500\mu\text{m}$ ) is common to all images.

month) and showed similar histological results. There was only 1 rat receiving a 5 MB graft that survived and had a patent graft (at 1 month). There were 4 rats in the 20 MB group that survived and had patent grafts, 2 of which were recovered at 1 month and showed similar histological results. At either 1, 3 or 6 months post-operatively the grafts and adjacent native blood vessels were harvested for histological evaluation. Patent grafts were recovered for every silk extraction condition. The native vessel was inspected histologically at points distal and proximal to the anastomosis and were found to be typical in appearance (data not shown). Graft cross sections were processed histologically and assessed for pore wall morphology, tissue deposition, cell phenotype and inflammatory responses.

In order to extend our previous findings [14], 20 MB formulations were first taken out to 6 months with interim explants at 1 and 3 months (Fig. 6). Verhoff's and trichrome staining indicated that abundant elastic fibers and collagen, respectively, were present throughout the time course of the study and localized to the interior of the graft walls and adventitia surrounding the 20 MB grafts. Comparatively little extracellular matrix was visualized within the pore walls of the 20 MB formulation, until 6 months when larger voids had formed in the pore wall, facilitating cellular and extracellular tissue ingrowth. Most of the graft remodeling seemed to occur between months 3 and 6, though the graft wall became progressively thinner and more compact over time.

Host cells rapidly migrated along the entire 10–15 mm graft inner

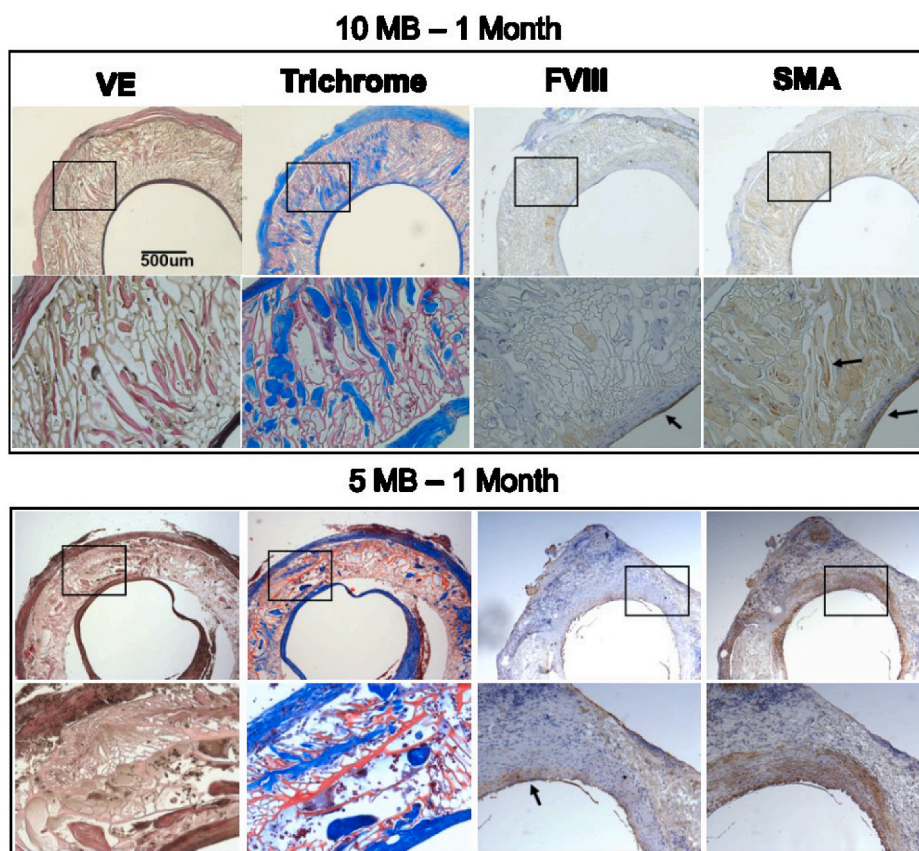


**Fig. 7.** Histological cross-sections of 10 MB (top) and 5 MB grafts 1-month post-implantation. Adjacent sections were stained for Verhoff's elastic (VE), trichrome, Factor VIII (FVIII) and smooth muscle actin (SMA). For each stain images are shown in low (20x, top) and high magnification (40x, bottom) corresponding to the box in the image above. Arrows indicate areas of clear positive IHC staining. Histology images shown were taken midgraft. The scale bar (500  $\mu\text{m}$ ) is common to all images.

lumen within 1 month and created a confluent endothelium (FVIII stain) which persisted for 6 months. Concurrently, smooth muscle cells were co-located with the areas of most well-developed elastic tissue, mostly found in the interior of the graft wall and with sparse staining in the outer adventitia. H&E staining indicated uniform cellularity along the graft exterior surface with no clear formation of any multi-nucleated foreign body giant cells (Fig. 9), suggesting the silk material was well-tolerated and did not elicit persistent inflammatory reactions. CD31 staining confirmed localization of endothelial cells and indicated very minimal persistence of acute inflammatory neutrophils or monocytes at any time point (Fig. 9). In contrast to the response to the 20 MB graft, the higher porosity grafts (5 and 10 MB) had much more pronounced cell and tissue infiltration into the pore walls by 1 month (Fig. 7). Verhoff's and trichrome staining revealed significant tissue deposition in dense pockets within the pore walls of the 10 MB graft.

This tissue was more continuously deposited across the entire wall of the 5 MB grafts, in addition to the adventitia surrounding the graft. In both 5 and 10 MB grafts the presence of smooth muscle and endothelial cells were again biased towards the inner lumen; however, in contrast to the 20 MB grafts, the more porous grafts enabled cell infiltration to occur earlier and far more abundantly. CD31 and H&E staining of the 5 and 10 MB grafts appeared similar to the 20 MB grafts at 1 month in terms of the cell types present and overall inflammatory responses to the graft (Fig. 9). The 5 MB grafts showed signs of mechanical failure at the suture walls, which limited further investigation of more implants at later time points. This behavior was attributed to the *in vitro* characterization which showed that highest molecular weight formulations (5 MB and 10 MB) were more compliant but had the lower suture retention strength.

#### 4. Discussion

The gel-spinning process was directly influenced by molecular weight; therefore, spinnable concentration ranges were identified across a wide range of molecular weights to define new processing windows for structure control. It has been established that porosity of graft materials can enhance cellular infiltration, with higher porosity leading to endothelialization and higher long term patency (up to 6 months) [31]. While some vascular grafting studies using ePTFE suggested that pores  $> 30 \mu\text{m}$  (as defined by inter-nodal distance of the fabric) promoted maximal patency in baboons and [1,32,33] later studies in dogs using PU grafts with more defined and interconnected pores suggested that pore sizes of 5–30  $\mu\text{m}$  could also promote enhanced patency compared to non-porous equivalents [31]. Designing grafts with bigger more interconnected pores, lead to thinner less dense pore walls. Pore wall thickness and porosity are hard to control independently of each other and more work is needed to decouple these factors from each other, though controlling the temperature and rate of freezing are potentially options worth further exploration. In prior studies described above, improved patency was attributed to improved transmural recruitment of endothelial cells, which was facilitated by enlarged routes of cell ingress. Interestingly, when compared side-by-side in a rat interpositional model [14], 30  $\mu\text{m}$ -pore-sized PU grafts encouraged more rapid endothelial coverage than their ePTFE counterparts, suggesting that interconnected and regular pores distributed through a graft luminal matrix may be more favorable than the textile architecture of commercially available ePTFE and Dacron grafts.

There is an agreement within the field that mechanical incompatibility of grafts leads to wall weakening, loss of endothelial cells, dilation at anastomosis, intimal hyperplasia and thrombus formation [34].

In this dynamic mechanical environment, graft compliance and strength must be in balance so as to conserve the optimal hemodynamic shear stresses within the vessel [35]. It has been shown that even small disturbances in the mechanical environment can make a vessel mechanically unstable. Mismatch in compliance can result in a mechanically unstable environment disturbing the local cell mechanical environment and lead to aneurysm or occlusions [36,37]. These factors are exacerbated in small diameter grafts where there is low flow blood and any impedance in flow can easily lead to occlusions. The mechanical properties of native and graft materials for vessel regeneration have been widely studied [38]. The trend in mechanical properties of common graft materials are balanced between strength and compliance with synthetic materials with elastic moduli in the GPa and MPa ranges resulting in low compliance (1–5 radial change per mm Hg  $\times 10^{-2}$ ) but high burst pressures ( $\sim 1000$ 's of mm Hg) [34,35,38]. These materials are used for replacement of large diameter vessels where high burst pressures (2000–5000 mm Hg) are needed but still are not able to match native compliance ( $\sim 20$  radial change per mm Hg  $\times 10^{-2}$ ). For small diameter grafts their stiffness causes significant mismatch in compliance. Natural protein based grafts [39–44] and optimized synthetic materials [45,46] can be optimized to have lower elastic moduli (0.1–10 MPa) and therefore higher compliance levels that can match gold standard (saphenous vein) for small diameter vessels ( $\sim 4$  radial change per mm Hg  $\times 10^{-2}$ ). These grafts also have suture retention strength similar to the gold standard ( $\sim 2.5$ – $3$  N) [47]. In the present work it was demonstrated that graft mechanical properties could be controlled by molecular weight and concentration. Modified mechanical properties of the tubes were attributed to both changes in polymer lengths constituting the matrix of the pore walls and the porosity of the resulting structure. With high porosity and low molecular weight, the graft structure was more flexible with lower elastic moduli (1 MPa), higher compliance (3.3 radial change per mm Hg  $\times 10^{-2}$ ) but low suture retention strength (0.25 N). While the results of compliance modeling suggest a route to obtain tissue-matched properties with more porous tubes, their lower suture retention strength enhance surgical risk and propensity for long-term mechanical failure. These systems provide a new basis to evaluate factors which may influence the patency of small-diameter tubes in ongoing small animal studies. Future studies can use these initial results and models to optimize the material or create composites to further increase elasticity while retaining strength. Future studies should also characterize the performance of grafts under cyclic deformation to understand whether grafts can resist long term deformation.

The use of constitutive and structural models that predict mechanical response have been thoroughly developed for natural vessels [48] and graft materials [49]. These models range from computational fluid dynamic models to analyze fluid flow, finite element analysis [49,50] to understand case specific mechanical predictions, to more complex numerical tools that employ hyper elastic models [51] and structure-fluid interactions [52]. In this work an analytical and FEA model was created with some basic assumptions to predict mechanical properties-based on quantifiable material parameters for a natural biopolymer. As such this model can be easily translated to different material formats, composites or a variety of geometries. Similar approaches have been taken with synthetic materials [53] such as aliphatic polyurethane [54], by using constituent material properties and both analytically and via FEA predicting the graft burst pressure and compliance. Castillo-Cruz's analytical and FEA model for circumferential strain and compliance was also based on the elastic properties of the constitutive material (elastic modulus and Poisson's ratio). The compliance of synthetic grafts was low (1.05%/100 mm Hg $^{-1}$ ) and was attributed to the stiffness of the material (elastic modulus of 4.63 MPa). Similar approaches have also been taken with biopolymer composites using FEA models [55] to predict compliance based on material properties and graft dimensions. Other groups [56] have used silk reinforced gelatin scaffolds whose elastic moduli could be tuned by controlling percentage of silk. Through

FEA they found their optimal formulation required a low elastic modulus of 0.1 MPa and graft thickness of 3 mm to reach comparable levels of compliance to native arteries. However, they found that by decreasing the stiffness of the grafts this resulted in lower mechanical strength leading to burst pressures at lower than physiological pressures.

The model created in this work was based on elastic theory of thick-walled cylinders had some limitations and took certain assumptions (a smooth cylindrical geometry and an assumption of linear elastic and isotropic material). The lyophilized silk material showed a linear behavior at physiological strain (around 1%). However, the porous structure of material was not considered. To improve model accuracy a hyper foam model [57] that takes graft geometry and porosity (via 3D scanning) into account could be developed. Analytical models for closed and open cell foams [58] could also be implemented to better understand the behavior of this porous material. These models can help elucidate the connectivity of the material in the porous network and further understand its mechanical behavior. Finally, edge effects of the anastomosis were ignored in the current model, which for design purposes was practical. The graft dimensions used for the model were: 10–15 mm length, 1.29 mm inner diameter, 0.1–0.2 mm thickness. Using these dimensions, the radius to thickness ratio would be  $\sim 10$  and thickness to length ratio would be  $\sim 100$ . Under these condition edge effects should be insignificant. While beyond the scope of this work considering stress concentrations at the anastomosis site could still improve predictions of performance *in vivo*.

*In vivo* results show that increase in porosity led to accelerated graft remodeling via higher cellular infiltration and tissue deposition. All implanted grafts showed good development of neointima and the presence of mature smooth muscle and endothelial cells forming a confluent endothelium at 1 month which remained intact up to 6 months. The presence of these phenotypes over 6-month time course indicate positive remodeling of the graft over time. While the graft wall progressively decreased in thickness over 6 months there was a concurrent increase in large voids, presumably from cell-mediated enzymatic breakdown of the silk matrix. The presence of smooth muscle and endothelial cells biased towards the inner lumen of the grafts indicated cells were not able to fully penetrate across the less porous graft wall, limiting integration. The lack of transmural tissue ingrowth was attributed to the density of the graft and further work should be done to create thinner walls while retaining the mechanical strength of the graft. Histology showed that higher molecular weight grafts had pore architecture that reflected those seen in SEM cross sections with greater pore size and interconnectivity throughout the entire thickness of the graft. As a result, in higher molecular weight (5 MB and 10 MB) grafts earlier and greater infiltration of cells and deposition of collagen through the graft wall was seen but tissue ingrowth was still biased towards the inner lumen. For the higher porosity tubes (higher molecular weight 5 MB and 10 MB) no patent grafts were seen past 1 month. These grafts showed signs of mechanical failure at the suture walls which potentially led to infiltration of inflammatory cells, platelet deposition and eventual activation of the clotting cascade leading to an occlusion. These *in vivo* observations matched the *in vitro* characterization which showed that highest molecular weight formulations (5 MB and 10 MB) were more compliant but had the lower suture retention strength. It appears tubes constructed of 10 MB silk contained the best balance of suture retention properties and cell infiltration properties. In our prior work [14], we evaluated the thrombogenic potential of silk compared to other materials *in vitro*. We found that the amount of protein adsorbed onto the silk films was lower than that of the PTFE films. We also observed platelets adhered to silk displayed a morphology close to that found on surfaces known to not activate platelets (collagen, BSA-coated glass). Future studies may focus on improving hemocompatibility of these more porous grafts or identifying layered or blended composites to improve long-term patency.

## 5. Conclusions

The goal of the present study was to optimize silk solution properties to enhance the porosity of gel-spun silk tubes. We hypothesized that more porous tubes composed of silk would degrade faster and improve rates of cellular ingress, while maintaining requisite mechanical functions, eventually improving host integration over time. Functional gel spinning was established across a range of silk concentrations and molecular weights. Degradation times *in vitro* increased with increasing molecular weight due to larger pores sizes and broader pore size distributions. Graft elasticity increased, and strength decreased as molecular weight and porosity increased. Material properties (elastic moduli) that resulted in optimal graft compliance for vascular applications were established but the lack of strength of these grafts led to difficulty deploying *in vivo*. However, this preliminary data could be used in the future to create bilayers and improve strength at anastomotic sites. Bilayer or composite grafts could be designed with a gradient of low molecular weight, higher strength at the ends (anastomotic sites) to higher molecular weight, higher porosity and more elastic formulations towards the middle of the grafts. These initial results further demonstrated the versatility in this silk gel spinning platform and underscored the importance of fine-tuning pore architecture in directing host integration in vascular systems.

## Acknowledgements

This work was supported by the NIH (NIH/NIBIB P41EB027062 and Diversity Supplement P41EB002520 - 11W1) and the American Heart Association (2012 Scholarship in Cardiovascular Disease and Stroke, M. Kluge).

## Appendix A. Supplementary data

Supplementary data to this article can be found online at <https://doi.org/10.1016/j.biomaterials.2019.119567>.

## References

- M.A. Golden, S.R. Hanson, T.R. Kirkman, P.A. Schneider, A.W. Clowes, Healing of polytetrafluoroethylene arterial grafts is influenced by graft porosity, *J. Vasc. Surg.* 11 (6) (1990) 838–844 discussion 845.
- A.W. Clowes, T.R. Kirkman, M.A. Reidy, Mechanisms of arterial graft healing. Rapid transmural capillary ingrowth provides a source of intimal endothelium and smooth muscle in porous PTFE prostheses, *Am. J. Pathol.* 123 (2) (1986) 220–230.
- Z. Zhang, Z. Wang, S. Liu, M. Kodama, Pore size, tissue ingrowth, and endothelialization of small-diameter microporous polyurethane vascular prostheses, *Biomaterials* 25 (1) (2004) 177–187, [https://doi.org/10.1016/S0142-9612\(03\)00478-2](https://doi.org/10.1016/S0142-9612(03)00478-2).
- H. Bergmeister, et al., Healing characteristics of electrospun polyurethane grafts with various porosities, *Acta Biomater.* 9 (4) (2013) 6032–6040, <https://doi.org/10.1016/j.actbio.2012.12.009>.
- E.S. Gil, et al., Mechanical improvements to reinforced porous silk scaffolds, *J. Biomed. Mater. Res. A* 99 (1) (2011) 16–28, <https://doi.org/10.1002/jbm.a.33158>.
- R. Walden, J.L. Gilbert, J. Megerman, W.M. Abbott, Matched elastic properties and successful arterial grafting, *Arch. Surg.* 115 (10) (1980) 1166–1169.
- G.J. Wilson, D.C. MacGregor, P. Klement, B.A. Weber, A.G. Binnington, L. Pinchuk, A compliant Corethane/Dacron composite vascular prosthesis. Comparison with 4-mm ePTFE grafts in a canine model, *Am. Soc. Artif. Intern. Organs J.* 39 (3) (1993) M526–M531.
- T. Asakura, T. Tanaka, R. Tanaka, Advanced silk fibroin biomaterials and application to small-diameter silk vascular grafts, *ACS Biomater. Sci. Eng.* 8b01482 (2019), <https://doi.org/10.1021/acsbomaterials.8b01482>.
- A.E. Thurber, F.G. Omenetto, D.L. Kaplan, *In vivo* bioresponses to silk proteins, *Biomaterials* 71 (2015) 145–157, <https://doi.org/10.1016/j.biomaterials.2015.08.039>.
- D. Wang, H. Liu, Y. Fan, Silk fibroin for vascular regeneration, *Microsc. Res. Tech.* 80 (3) (2017) 280–290, <https://doi.org/10.1002/jemt.22532>.
- C. Holland, K. Numata, J. Rnjak-Kovacic, F.P. Seib, The biomedical use of silk: past, present, future, *Adv. Healthc. Mater.* 8 (1) (2019), [https://doi.org/10.1002/ADHM.201800465@10.1002/\(ISSN\)1097-0282.BIOPOLYMERS2019](https://doi.org/10.1002/ADHM.201800465@10.1002/(ISSN)1097-0282.BIOPOLYMERS2019).
- M.L. Lovett, C.M. Cannizzaro, G. Vunjak-Novakovic, D.L. Kaplan, Gel spinning of silk tubes for tissue engineering, *Biomaterials* 29 (35) (2008) 4650–4657, <https://doi.org/10.1016/j.biomaterials.2008.08.025>.
- L. Soffer, et al., Silk-based electrospun tubular scaffolds for tissue-engineered vascular grafts, *J. Biomater. Sci. Polym. Ed.* 19 (5) (2008) 653–664, <https://doi.org/10.1163/156856208784089607>.
- M. Lovett, G. Eng, J.A. Kluge, C. Cannizzaro, G. Vunjak-Novakovic, D.L. Kaplan, Tubular silk scaffolds for small diameter vascular grafts, *Organogenesis* 6 (4) (2010), <https://doi.org/10.4161/org.6.4.13407> 217–24.
- L.S. Wray, et al., Effect of processing on silk-based biomaterials: reproducibility and biocompatibility, *J. Biomed. Mater. Res. B Appl. Biomater.* 99B (1) (2011) 89–101, <https://doi.org/10.1002/jbm.b.31875>.
- J.A. Kluge, B.T. Kahn, J.E. Brown, F.G. Omenetto, D.L. Kaplan, Optimizing molecular weight of lyophilized silk as a shelf-stable source material, *ACS Biomater. Sci. Eng.* 2 (4) (2016) 595–605.
- P. Zilla, D. Bezuidenhout, P. Human, Prosthetic vascular grafts: wrong models, wrong questions and no healing, *Biomaterials* 28 (34) (2007) 5009–5027, <https://doi.org/10.1016/J.BIOMATERIALS.2007.07.017>.
- D.N. Rockwood, R.C. Preda, T. Yücel, X. Wang, M.L. Lovett, D.L. Kaplan, Materials fabrication from Bombyx mori silk fibroin, *Nat. Protoc.* 6 (10) (2011) 1612–1631, <https://doi.org/10.1038/nprot.2011.379>.
- L.S. Wray, et al., Effect of processing on silk-based biomaterials: reproducibility and biocompatibility, *J. Biomed. Mater. Res. B Appl. Biomater.* 99 (1) (2011) 89–101, <https://doi.org/10.1002/jbm.b.31875>.
- J. Rnjak-Kovacic, et al., Lyophilized Silk Sponges: A Versatile Biomaterial Platform for Soft Tissue Engineering, (2015).
- J.A. Kluge, B.T. Kahn, J.E. Brown, F.G. Omenetto, D.L. Kaplan, Optimizing Molecular Weight of Lyophilized Silk as a Shelf-Stable Source Material, (2016).
- Y.-C. Fung, Mechanical properties and active remodeling of blood vessels, *Biomechanics*, Springer, 1993, pp. 321–391.
- Cardiovascular Implants and Extracorporeal Systems - Vascular Prostheses - Tubular Vascular Grafts and Vascular Patches, ISO 7198:2016, 2016.
- Compliance of abdominal aortic aneurysms before and after stenting with tissue Doppler imaging: evolution during follow-up and correlation with aneurysm diameter, *Ann. Vasc. Surg.* 23 (1) (2009) 49–59, <https://doi.org/10.1016/J.AVSG.2008.08.006>.
- N. L'Heureux, et al., Human tissue-engineered blood vessels for adult arterial revascularization, *Nat. Med.* 12 (3) (2006) 361–365, <https://doi.org/10.1038/nm1364>.
- Z.-Y. Li, S. Howarth, M. Graves, J.H. Gillard, Measurement of stenotic carotid arterial compliance with MRI, 2008 30th Annual International Conference of the IEEE Engineering in Medicine and Biology Society, 2008, pp. 1403–1406.
- J. Joseph, V. Jayashankar, A virtual instrument for real time *in vivo* measurement of carotid artery compliance, 2008 30th Annual International Conference of the IEEE Engineering in Medicine and Biology Society, 2008, pp. 2281–2284.
- Mechanical behavior of polyurethane-based small-diameter vascular grafts, (2016) 451–477.
- N. Jirofti, D. Mohebbi-Kalhor, A. Samimi, A. Hadjizadeh, G.H. Kazemzadeh, Small-diameter vascular graft using co-electrospun composite PCL/PU nanofibers, *Biomed. Mater.* 13 (5) (2018) 055014, <https://doi.org/10.1088/1748-605X/aad4b5>.
- M.A. Hiob, S. She, L.D. Muiznieks, A.S. Weiss, Biomaterials and modifications in the development of small-diameter vascular grafts, *ACS Biomater. Sci. Eng.* 3 (5) (2017) 712–723, <https://doi.org/10.1021/acsbomaterials.6b00220>.
- C.D. Campbell, D.H. Brooks, M.W. Webster, H.T. Bahnsen, The use of expanded microporous polytetrafluoroethylene for limb salvage: a preliminary report, *Surgery* 79 (5) (1976) 485–491.
- J.B. Campbell, J.L. Glover, B. Herring, The influence of endothelial seeding and platelet inhibition on the patency of ePTFE grafts used to replace small arteries—an experimental study, *Eur. J. Vasc. Surg.* 2 (6) (1988) 365–370, [https://doi.org/10.1016/S0950-821X\(88\)80013-6](https://doi.org/10.1016/S0950-821X(88)80013-6).
- H.J. Salacinski, et al., The mechanical behavior of vascular grafts: a review, *J. Biomater. Appl.* 15 (3) (2001) 241–278, <https://doi.org/10.1106/NA5T-J57A-JTDD-FD04>.
- P.M. Crapo, Y. Wang, Physiologic compliance in engineered small-diameter arterial constructs based on an elastomeric substrate, *Biomaterials* 31 (7) (2010) 1626–1635, <https://doi.org/10.1016/J.BIOMATERIALS.2009.11.035>.
- M.S. Hanh, Chapter 7: mechanical stimulation and biomimetic scaffolds for tissue engineered vascular grafts, in: N. Ashammakhi, R. Reis, F. Chiellini (Eds.), *Topics in Tissue Engineering*, 2008 College Station.
- E.E. van Haften, C.V.C. Bouten, N.A. Kurniawan, Vascular mechanobiology: towards control of *in situ* regeneration, *Cells* 6 (3) (2017), <https://doi.org/10.3390/CELLS6030019>.
- R.L. Gleason, J.-J. Hu, J.D. Humphrey, Building a functional artery: issues from the perspective of mechanics, *Front. Biosci.* 9 (2004) 2045–2055.
- F.P. Seib, M. Herklotz, K.A. Burke, M.F. Maitz, C. Werner, D.L. Kaplan, Multifunctional silk-heparin biomaterials for vascular tissue engineering applications, *Biomaterials* 35 (1) (2014) 83–91, <https://doi.org/10.1016/j.biomaterials.2013.09.053>.
- A. Aytemiz, et al., Small-diameter silk vascular grafts (3 mm diameter) with a double-raschel knitted silk tube coated with silk fibroin sponge, *Adv. Healthc. Mater.* 2 (2) (2013) 361–368, <https://doi.org/10.1002/adhm.201200227>.
- D. Smoot, *Functionalization and Characterization of Silk Based Gel-Spun Vascular Grafts*, Tufts University, 2015.
- J.D. Berglund, R.M. Nerem, A. Sambanis, Incorporation of intact elastin scaffolds in tissue-engineered collagen-based vascular grafts, *Tissue Eng.* 10 (9–10) (2004) 1526–1535, <https://doi.org/10.1089/ten.2004.10.1526>.
- C. Xu, R. Inai, M. Kotaki, S. Ramakrishna, Aligned biodegradable nanofibrous structure: a potential scaffold for blood vessel engineering, *Biomaterials* 25 (5) (2004) 877–886, [https://doi.org/10.1016/S0142-9612\(03\)00593-3](https://doi.org/10.1016/S0142-9612(03)00593-3).

- [44] F. Boccafoschi, J. Habermehl, S. Vesentini, D. Mantovani, Biological performances of collagen-based scaffolds for vascular tissue engineering, *Biomaterials* 26 (35) (2005) 7410–7417, <https://doi.org/10.1016/j.biomaterials.2005.05.052>.
- [45] K.H. Lee, H.Y. Kim, M.S. Khil, Y.M. Ra, D.R. Lee, Characterization of nano-structured poly( $\epsilon$ -caprolactone) nonwoven mats via electrospinning, *Polymer* 44 (4) (2003) 1287–1294, [https://doi.org/10.1016/S0032-3861\(02\)00820-0](https://doi.org/10.1016/S0032-3861(02)00820-0).
- [46] J. Guo, M. Zhao, Y. Ti, B. Wang, Study on structure and performance of polycarbonate urethane synthesized via different copolymerization methods, *J. Mater. Sci.* 42 (14) (2007) 5508–5515, <https://doi.org/10.1007/s10853-006-1024-5>.
- [47] L. Soletti, et al., A bilayered elastomeric scaffold for tissue engineering of small diameter vascular grafts, *Acta Biomater.* 6 (1) (2010), <https://doi.org/10.1016/j.actbio.2009.06.026> 110–22.
- [48] R.P. Vito, S.A. Dixon, Blood vessel constitutive models 1995–2002, *Annu. Rev. Biomed. Eng.* 5 (1) (2003) 413–439, <https://doi.org/10.1146/annurev.bioeng.5.011303.120719>.
- [49] M.A. Jankowska, M. Bartkowiak-Jowska, R. Bedzinski, Experimental and constitutive modeling approaches for a study of biomechanical properties of human coronary arteries, *J. Mech. Behav. Biomed. Mater.* 50 (1–12) (2015), <https://doi.org/10.1016/J.JMBBM.2015.05.021>.
- [50] F. Nappi, et al., Compliance mismatch and compressive wall stresses drive anomalous remodelling of pulmonary trunks reinforced with Dacron grafts, *J. Mech. Behav. Biomed. Mater.* 63 (2016) 287–302, <https://doi.org/10.1016/J.JMBBM.2016.06.023>.
- [51] C.A. Bustos, C.M. García-Herrera, D.J. Celentano, Modelling and simulation of the mechanical response of a Dacron graft in the pressurization test and an end-to-end anastomosis, *J. Mech. Behav. Biomed. Mater.* 61 (2016) 36–44, <https://doi.org/10.1016/J.JMBBM.2016.01.005>.
- [52] S.F.C. Stewart, D.J. Lyman, Effects of an artery/vascular graft compliance mismatch on protein transport: a numerical study, *Ann. Biomed. Eng.* 32 (7) (2004) 991–1006, <https://doi.org/10.1023/B:ABME.0000032462.56207.65>.
- [53] F. Montini-Ballarín, et al., Mechanical behavior of bilayered small-diameter nanofibrous structures as biomimetic vascular grafts, *J. Mech. Behav. Biomed. Mater.* 60 (2016) 220–233, <https://doi.org/10.1016/J.JMBBM.2016.01.025>.
- [54] O. Castillo-Cruz, C. Pérez-Aranda, F. Gamboa, J.V. Cauich-Rodríguez, D. Mantovani, F. Avilés, Prediction of circumferential compliance and burst strength of polymeric vascular grafts, *J. Mech. Behav. Biomed. Mater.* 79 (2018) 332–340, <https://doi.org/10.1016/j.jmbbm.2017.12.031>.
- [55] S. Harrison, E. Tamimi, J. Uhlorn, T. Leach, J.P. Vande Geest, Computationally optimizing the compliance of a biopolymer based tissue engineered vascular graft, *J. Biomech. Eng.* 138 (1) (2016), <https://doi.org/10.1115/1.4032060>.
- [56] F. Couet, D. Mantovani, Experimental validation of a new approach for the development of mechano-compatible composite scaffolds for vascular tissue engineering, *J. Mater. Sci. Mater. Med.* 19 (7) (2008) 2551–2554, <https://doi.org/10.1007/s10856-007-3242-z>.
- [57] M.S. Sirry, P. Zilla, T. Franz, A computational study of structural designs for a small-diameter composite vascular graft promoting tissue regeneration, *Cardiovasc. Eng. Technol.* 1 (4) (2010) 269–281, <https://doi.org/10.1007/s13239-010-0023-5>.
- [58] L.J. Gibson, M.F. Ashby, *Cellular Solids*, Cambridge University Press, Cambridge, 1997.